

Effects of velocity-dependent apparent toughness on the pre- and post-shut-in growth of a hydraulic fracture

Dong Liu^a, Guanyi Lu^b

^a*Department of Earth Sciences, University College London, 5 Gower Place, London WC1E 6BS, UK*

^b*Gaznat chair on Geo-Energy, Institute of Civil Engineering, École Polytechnique Fédérale de Lausanne (EPFL), Lausanne, Switzerland*

Abstract

We investigate the growth of a plane-strain/radial hydraulic fracture in an infinite impermeable medium driven by a constant injection rate assuming that the apparent toughness scales with the decreasing fracture growth rate in a power-law relation. The viscosity dominated regime always governs the fracture growth at large time for the plane-strain geometry. For a radial hydraulic fracture, we report a transition from early-time fracture growth dominated by viscous fluid flow to large-time propagation dominated by fracture toughness. Such a transition results from an overall increase of the energy dissipation by fracture surface creation. After shut-in, both plane-strain and radial fractures propagate at a lower velocity with decreasing fracture toughness. The fracture growth then depends on the dimensionless toughness at the stop of fluid injection and transitions towards a self-similar pulse-viscosity solution when viscous fluid flow dominates the energy dissipation. The fracture arrests when fulfilling two conditions – the apparent toughness reaching its minimum, and viscous forces being negligible in the fluid flow. The fracture dimension at arrest is independent of the velocity-dependent power-law relation.

Keywords: Hydraulic fracture, Rate-dependent toughness, Sub-critical fracture growth, Gauss-Chebyshev quadrature, Barycentric interpolations

1. Introduction

Fracture growth presents a rate sensitivity in many materials, such as cement (Bažant and Gettu, 1992), rocks (Atkinson, 1984; Atkinson and Meredith, 1987; Ponson, 2009), glass and ce-

*Corresponding author: Dong Liu, dong.liu@ucl.ac.uk

ramics (Lawn, 1993), and polymers (Atkins et al., 1975; Sharon and Fineberg, 1999; Pohlitz et al., 2008; Goldman et al., 2010; Kwon et al., 2011). Such rate dependence of the fracture toughness will probably have a more significant influence on hydraulic fracture growth due to its strong coupling with the fluid injection rate. Despite of the wide existence of hydraulic fractures in nature (such as in the formation of magma-driven dikes and sills, and the drainage of glacier lakes) and in industrial applications (the preconditioning of mining, enhanced geothermal production, and hydrocarbon recovery to name a few), monitoring the fracture propagation rate remains challenging in rocks (Liu et al., 2020; Liu and Lecampion, 2022, 2023) and few studies have reported such rate-dependent characteristics of the hydraulic fracture growth (Chen et al., 2021). In this paper, we aim to analyze the growth of a fluid-driven fracture under the assumption of velocity-dependent apparent toughness hoping to help guide and interpret future observations in the laboratory and field.

Most dynamic (Wada et al., 1996; Bertram and Kalthoff, 2003; Zhang and Zhao, 2013; Gao et al., 2015; Zhao et al., 2017; Oh et al., 2019; Shi et al., 2019) or quasi-static fracture toughness characterization in the laboratory (Bažant and Gettu, 1992; Xu et al., 2004; Zhang and Zhao, 2013; Dai and Xia, 2013; Mahanta et al., 2017; Oh et al., 2019; Xing et al., 2020; Aliha et al., 2021) presents a velocity-toughening characteristic with an instant fracture propagation at around one tenth of the Rayleigh wave speed. Such toughening mechanism is related to the non-equilibrium nature of fracture problems at high crack speeds where inertia forces (Anderson, 2017) or material heterogeneities (Albertini et al., 2021) reduce the energy flow into the fracture tip and translate to larger fracture resistance. By controlling the fracture speed via crack opening displacement rate (Ponson, 2009; Vasudevan et al., 2021), fracture growth can be obtained with negligible inertia effects at much lower velocities. Depending on the material type, mechanisms related to the process zone (Chen et al., 2021), the creep and plastic deformation (Xu et al., 2004), and the viscoelastic and viscoplastic failure (Kwon et al., 2011) then become more important and lead to velocity-toughening (Bažant and Gettu, 1992; Chen et al., 2021) or -weakening (Xu et al., 2004; Aliha et al., 2021) fracture growth.

Velocity-dependent toughness has also been reported for the sub-critical fracture growth, where the fracture propagates in a stable and quasi-static manner at an apparent toughness much lower

than the critical fracture toughness. The sub-critical growth in rocks is associated with a low fracture velocity of around $10^{-16} - 10^{-2}$ m/s (Atkinson and Meredith, 1987) and results from multiple mechanisms such as atomic diffusion, dissolution, ion exchange, and microplasticity. Among these mechanisms, stress corrosion dominates under conditions prevailing in the upper crust (Branatut et al., 2013) and becomes more influential in the presence of water and aqueous solutions. It would be thus surprising that the propagation of hydraulic fractures is not under the influence of stress corrosion. As a matter of fact, the sub-critical fracture growth has been proposed as one of the fundamental mechanisms of the generation and propagation of multiple fractures simultaneously in multistage hydraulic fracturing stimulation (Lu et al., 2017).

Previous studies on hydraulic fracturing have accounted for velocity-dependent apparent toughness in the context of sub-critical fracture growth. These earlier investigations cover from the fracture initiation from a wellbore (Lu et al., 2017, 2020) to the fracture growth under uniform pressurization (Olson and Taleghani, 2009). However, a systematical study of the fracture growth regime transition over a large time scale is missing. Moreover, rate-dependent characteristics may have a larger impact on the post-shut-in growth of hydraulic fractures, during which the velocity decreases significantly compared with the propagation phase. As a result, the fracture behavior after shut-in probably deviates from constant toughness predictions (Garagash, 2006a; Möri and Lecampion, 2021; Peirce and Detournay, 2022a,b; Peirce, 2022). An earlier study (Möri and Lecampion, 2021) looks at the arrest of a radial fracture in the context of sub-critical growth and points out an significant increase of the fracture extension at arrest due to rate-dependent effects. However, such rate dependence has been neglected prior to the stop of fluid injection. Hydraulic fracture propagation with full consideration of rate-dependent effects throughout the fracturing process remains unknown.

In this paper, we adopt a generalized empirical power-law model of apparent toughness dependent on fracture velocity to describe the rate-sensitive fracture growth. We focus on its effects on the propagation of a plane-strain and a radial hydraulic fracture in an impermeable medium. We perform the dimensional analysis and analyze the transition of different propagation regimes over time via an efficient numerical solver based on the Gauss-Chebyshev quadrature and barycentric interpolation techniques (Liu et al., 2019). We also investigate the post-shut-in growth of hy-

draulic fractures and the fracture extensions at arrest by assuming the toughness dependent on velocity during the entire fracture growth.

2. Model description

Following the theory of linear elastic fracture mechanics, we consider here a negligible process zone size compared to fracture dimensions, and lump the effects of different mechanisms into one simple apparent toughness. A power-law or exponential relation may exist between the apparent toughness and fracture growth rate. We summarize some of the materials presenting such rate-dependent fracture toughness in Table 1. This rate dependence however can be approximated by different power-law or exponential relations at different velocity ranges – the low crack speed related to the sub-critical growth (Atkinson, 1984; Ponson, 2009), the medium speed during the stable/static fracture propagation (Ponson, 2009; Vasudevan et al., 2021) and the high speed attributed to dynamic fracture growth (Zhang and Zhao, 2013; Scheibert et al., 2010). In this paper, we neglect the influence of fracture velocity range and use a generalized power-law relation in the form of Charles’ law (Charles, 1958) for all crack speed.

$$K_{Ic} = B(d\ell/dt)^\alpha, \quad B = \frac{K_*}{v_*^\alpha} \quad (1)$$

where K_* is the apparent fracture toughness at a given fracture growth rate/velocity of v_* . Such a power-law dependence does not introduce any new length scale as the pair of v_* and K_* is selected so as to characterize the velocity dependence of the apparent toughness. $\alpha > 0$ is the power-law scaling exponent. For most rocks, we have $\alpha \approx 0.005 - 0.1$ (Atkinson, 1984; Atkinson and Meredith, 1987; Olson, 2004). For PMMA, this value is $\alpha = 0.096$ (Vasudevan et al., 2021).

	Materials and velocity range
Power-law like relation	Marble ($v = 400 - 1000$ m/s) (Zhang and Zhao, 2013)
	Laurentian granite ($v = 200 - 1000$ m/s) (Gao et al., 2015)
	High-strength steel ($v = 1 - 1100$ m/s) (Rosakis and Zehnder, 1985; Anderson, 2017)

	PMMA ($\nu = 10^{-7} - 10$ m/s) (Atkins et al., 1975; Vasudevan et al., 2021) ($\nu = 100 - 400$ m/s) (Scheibert et al., 2010)
	Sandstone ($\nu = 0.01 - 1$ m/s) (Ponson, 2009)
	Calcite, quartzite, granitic and basic rocks ($\nu = 10^{-16} - 10^{-2}$ m/s) (Charles, 1958; Atkinson, 1984; Atkinson and Meredith, 1987)
	Cross-linked hydrogel ($\nu = 10^{-4} - 3 \times 10^{-2}$ m/s) (Baumberger et al., 2006)
Exponential like relation	Sandstone ($\nu = 10^{-5} - 10^{-2}$ m/s) (Ponson, 2009)
	Quartz ($\nu = 10^{-8} - 10^{-2}$ m/s) (Darot and Gueguen, 1986)
	Glass, ceramics ($\nu = 10^{-12} - 10^{-1}$ m/s) (Freiman, 1984; Wan et al., 1990; Lawn, 1993)

Table 1: Examples of materials showing rate-dependent apparent fracture toughness.

3. Mathematical formulation

We introduce a parameter d to represent the mathematical formulations of a plane-strain ($d = 1$) and a radial hydraulic fracture ($d = 2$). Following Savitski and Detournay (2002); Detournay (2004); Liu et al. (2019), we use the following set of effective material parameters for clarity:

$$K' = \sqrt{\frac{32}{\pi}} K_*, \quad E' = \frac{E}{1 - \nu^2}, \quad \mu' = 12\mu \quad (2)$$

where E is the solid elastic modulus, ν Poisson's ratio, μ the fluid viscosity, and K_* the reference apparent fracture toughness corresponding to $\nu = \nu_*$.

3.1. Elasticity

The elasticity relates the fracture opening w and the net pressure $p = p_f - \sigma_o$ (σ_o is the in-situ compressive stress normal to the fracture plane) via a singular boundary integral equation (Hills et al., 2013).

$$\frac{1}{4\pi} \frac{1}{\ell} \int_{-1}^1 G_d(\xi, \xi') \frac{\partial w}{\partial \xi'} d\xi' = \frac{1}{E'} p, \quad \xi \in [-1, 1] \quad (3)$$

where $\xi = x/\ell$ is the dimensionless spatial coordinate in the fracture. $\ell(t)$ denotes the fracture half-length in plane-strain, and the fracture radius for the radial geometry. G_d is the elastic kernel which represents the stress component normal to the fracture plane induced by a unit dislocation. It is of course a function of the fracture geometry:

- Plane-strain ($d = 1$)

$$G_1(\xi, \xi') = \frac{1}{\xi - \xi'} \quad (4)$$

- Radial ($d = 2$)

$$G_2(\xi, \xi') = \begin{cases} \text{sign}(\xi\xi') \left[\frac{1}{\xi - \xi'} \mathbf{E}(h) - \frac{1}{\xi} \mathbf{K}(h) \right], & |\xi'| < |\xi| \\ \frac{1}{\xi - \xi'} \mathbf{E}(1/h), & |\xi'| > |\xi| \end{cases} \quad (5)$$

where $h = \xi'/\xi$ and $\mathbf{E}(h)$ and $\mathbf{K}(h)$ denote the complete elliptic integrals (Cleary and Wong, 1985; Gordeliy and Detournay, 2011; Liu et al., 2019).

3.2. Lubrication flow

Under the assumption of zero fluid compressibility, zero fluid lag and zero leak-off, the width-averaged fluid mass conservation writes:

$$\frac{\partial w}{\partial t} + \frac{1}{x^{d-1}} \frac{\partial}{\partial x} (x^{d-1} q) = 0 \quad (6)$$

where q is the local fluid flux which is expressed as Poiseuille's law under laminar flow conditions (Batchelor, 2000):

$$q = -\frac{w^3}{\mu'} \frac{\partial p}{\partial x} \quad (7)$$

3.3. Boundary conditions

The fracture tip $x = \ell$ is characterized by zero fluid flux and zero fracture opening (Detournay and Peirce, 2014):

$$q(\ell) = 0, \quad w(\ell) = 0 \quad (8)$$

3.4. Global continuity equation

We assume that the fluid is injected at the fracture center $x = 0$ with a volume of V . By integrating the lubrication equation (6) with the boundary conditions (8), we obtain a global fluid continuity equation inside the fracture.

$$2 \int_0^\ell (\pi x)^{d-1} w dx = V \quad (9)$$

In the context of a constant injection rate Q_o , we have

$$V = Q_o t, \quad 2 \lim_{x/\ell \rightarrow 0} (\pi x)^{d-1} q = Q_o \quad (10)$$

3.5. Propagation criterion

Assuming a negligible process zone compared to the fracture length, we follow the linear elastic fracture mechanics by introducing an apparent fracture toughness to describe the rate-dependent characteristics of the fracture growth. The propagation criterion of a hydraulic fracture then translates into the classical square-root asymptote near the fracture tip (Rice, 1968), with the mode I stress intensity factor K_I equal to the fracture toughness K_{Ic} at all time: $K_I = K_{Ic}$. In view of the velocity-dependent evolution of the toughness described by the power law in Eq. (1), the asymptote for fracture width near the tip becomes:

$$w \sim \frac{K'}{E'} (\ell - x)^{1/2} \left(\frac{\dot{\ell}}{v_*} \right)^\alpha, \quad 1 - x/\ell \ll 1$$

4. Scaling analysis and structure of solutions

4.1. Viscosity and toughness scaling

The propagation of plane-strain and radial hydraulic fractures are well-understood for velocity-independent fracture toughness (Savitski and Detournay, 2002; Garagash and Detournay, 2005; Garagash, 2006b). When neglecting the fluid lag, leak-off, and system compressibility, the structure of solutions depends on two scaling relations: the viscosity dominated regime (M -regime) associated with the energy dissipation dominated by the viscous fluid flow, and the toughness dominated regime (K -regime), whose energy dissipation is dominated by the creation of fracture surfaces. A single dimensionless parameter \mathcal{K} (denoted as the dimensionless toughness) is able

to characterize the relative importance of toughness versus viscous forces. Such dimensionless toughness is constant for a plane-strain fracture since the energy associated with fracture surface creation comes solely from the two propagating tips and does not evolve with time. It however increases with time for a radial fracture due to an increasing fracture front perimeter as the fracture extends. As a result, the radial fracture always transitions from the viscosity dominated regime at early time to the toughness dominated regime at large time. In what follows, we investigate the scaling relations for plane-strain and radial hydraulic fractures accounting for a velocity-dependent fracture toughness assuming zero compressibility, zero leak-off, and zero fluid lag. We also discuss its differences compared to constant fracture toughness.

We introduce a dimensionless fracture opening Ω , net pressure Π , and fracture half-length or fracture radius γ as follows:

$$\ell(t) = L(t)\gamma(\mathcal{G}), \quad w(x, t) = \epsilon(t)L(t)\Omega(\xi, \mathcal{G}), \quad p(x, t) - \sigma_o = \epsilon(t)E'\Pi(\xi, \mathcal{G}), \quad \dot{\ell}(t) = \frac{L(t)}{t}\mathcal{V}(\mathcal{G}) \quad (11)$$

where $\epsilon(t)$ is a small dimensionless parameter capturing the fact that the fracture characteristic scale $W(t) = \epsilon(t)W(t)$ is much smaller than the characteristic length $L(t)$ and that the net pressure $P(t) = \epsilon(t)E'$ is much smaller than the rock elastic modulus. \mathcal{V} is the time-dependent dimensionless fracture velocity. $\mathcal{G}(t)$ denotes additional dimensionless parameters of which the solutions depend on.

Using such definitions, we obtain the following dimensionless form of the governing equations.

- Elasticity

$$\frac{1}{4\pi} \frac{1}{\gamma} \int_{-1}^1 G_d(\xi, \xi') \frac{\partial \Omega}{\partial \xi'} d\xi' = \Pi(\xi) \quad (12)$$

- Lubrication flow

$$\left(\frac{\dot{\epsilon}t}{\epsilon} + \frac{\dot{L}t}{L} \right) \Omega - \frac{\dot{L}t}{L} \xi \frac{\partial \Omega}{\partial \xi} + \dot{\mathcal{G}}t \left(\frac{\partial \Omega}{\partial \mathcal{G}} - \frac{\xi}{\gamma} \frac{d\gamma}{d\mathcal{G}} \frac{\partial \Omega}{\partial \xi} \right) = \frac{1}{\mathcal{G}_m} \frac{1}{\gamma^2 \xi^{d-1}} \frac{\partial}{\partial \xi} \left(\xi^{d-1} \Omega^3 \frac{\partial \Pi}{\partial \xi} \right) \quad (13)$$

- Global continuity equation

$$2\pi^{d-1} \gamma^d \int_0^1 \xi^{d-1} \Omega d\xi = \mathcal{G}_v \quad (14)$$

- Propagation condition:

$$\Omega \sim \mathcal{G}_k \gamma^{1/2} (1 - \xi)^{1/2} \mathcal{V}^\alpha, \quad 1 - \xi \ll 1 \quad (15)$$

\mathcal{G}_m , \mathcal{G}_v and \mathcal{G}_k are three independent dimensionless groups obtained respectively from the lubrication flow, global continuity and propagation criterion:

$$\mathcal{G}_v = \frac{V}{\epsilon L^{d+1}}, \quad \mathcal{G}_m = \frac{\mu'}{\epsilon^3 E' t}, \quad \mathcal{G}_k = \frac{K'}{\epsilon E' L^{1/2}} \left(\frac{L}{v_* t} \right)^\alpha \quad (16)$$

They all depend on time and will be defined depending on the importance of the corresponding governing equation. For an impermeable medium, the fracture volume always equals the injected volume, we therefore set $\mathcal{G}_v = 1$. We then obtain a viscosity (M -) and a toughness (K -) scaling relation by assuming either viscous fluid flow ($\mathcal{G}_m = 1$) or toughness ($\mathcal{G}_k = 1$) dominates. We show the characteristic scales and dimensionless parameters of these two scaling relations (M - and K -scaling) in Table 2.

Scaling	$M, M^{[V]} \quad (\mathcal{G}_m = 1)$	$K, K^{[V]} \quad (\mathcal{G}_k = 1)$
$\epsilon(t)$	$\left(\frac{\mu'}{E' t} \right)^{1/3}$	$\left(\frac{V^{\alpha-1/2} K'^{d+1}}{E'^{d+1} v_*^{\alpha(d+1)} t^{\alpha(d+1)}} \right)^{1/(\alpha+d+1/2)}$
$L(t)$	$\left(\frac{E' V^3 t}{\mu'} \right)^{1/(3(d+1))}$	$\left(\frac{E' V v_*^\alpha t^\alpha}{K'} \right)^{1/(\alpha+d+1/2)}$
$W(t)$	$\left(\frac{\mu'^d V^3}{E'^d t^d} \right)^{1/(3(d+1))}$	$\left(\frac{V^{\alpha+1/2} K'^d}{E'^d v_*^\alpha t^{\alpha d}} \right)^{1/(\alpha+d+1/2)}$
$P(t)$	$\left(\frac{E'^2 \mu'}{t} \right)^{1/3}$	$\left(\frac{V^{\alpha-1/2} K'^{d+1}}{E'^{1/2-\alpha} v_*^{\alpha(d+1)} t^{\alpha(d+1)}} \right)^{1/(\alpha+d+1/2)}$

Table 2: Viscosity and toughness scaling relations for plane-strain ($d = 1$) and radial ($d = 2$) hydraulic fractures for velocity-dependent toughness. M and K represent respectively the viscosity and toughness scaling relations under a constant injection rate where $V = Q_o t$. $M^{[V]}$ and $K^{[V]}$ represent the viscosity and toughness scaling relations for a finite volume pulse of $V = V_s$.

In the context of a constant injection rate Q_o , we define respectively the dimensionless parameter \mathcal{G} appearing in the M -scaling and K -scaling as the dimensionless toughness \mathcal{K} and dimensionless viscosity \mathcal{M} . They are related to one another and characterize the relative importance of

the energy dissipation by the creation of fracture surfaces over that by the viscous fluid flow or vice versa.

$$\mathcal{K} = \mathcal{M}^{-(\alpha+d+1/2)/(3(d+1))} = \left(\frac{t}{t_{mk}}\right)^{(\alpha-3\alpha d+d-1)/(3(d+1))}, \quad t_{mk} = \left(\frac{v_*^{3\alpha(d+1)} E'^{2d-\alpha+5/2} Q_o^{-3\alpha+3/2} \mu'^{\alpha+d+1/2}}{K'^{3(d+1)}}\right)^{1/(\alpha-3\alpha d+d-1)} \quad (17)$$

where the timescale t_{mk} , quantifies the time of transition between the M -regime and the K -regime at which characteristic fracture scales are equal to each other: $L_m(t_{mk}) = L_k(t_{mk}) = L_{mk}$, $W_m(t_{mk}) = W_k(t_{mk}) = W_{mk}$, and $P_m(t_{mk}) = P_k(t_{mk}) = P_{mk}$.

Note that only the toughness dominated scaling relation is modified compared to the case of the fracture velocity-independent toughness. When $\alpha = 0$, we recover the same viscosity and toughness scaling relations, and dimensionless toughness \mathcal{K} as the case of the velocity-independent toughness reported in Savitski and Detournay (2002); Garagash and Detournay (2005); Garagash (2006b).

4.2. Zero-viscosity / toughness dominated solutions

The viscosity dominated solutions remain the same for the case of a velocity-independent fracture toughness, which is already available in the literature (Savitski and Detournay, 2002; Garagash and Detournay, 2005). We thus derive here toughness dominated solutions by following the same procedure as that in Garagash (2000); Savitski and Detournay (2002); Liu et al. (2019) by assuming a spatially uniform pressure distribution inside the fracture. As a result, $\mathcal{K} = \infty$ does not evolve with time, and the dimensionless velocity is also time-independent.

$$\mathcal{V}_k = \gamma_k \frac{dL_k(t)/dt}{L_k(t)/t} = \gamma_k \left(\frac{\alpha + 1}{\alpha + d + 1/2}\right) \quad (18)$$

where the subscript k indicates the zero-viscosity solutions. The governing equations reduce to the elastic solution for a uniformly pressurized fracture, global volume balance and fracture propagation condition:

$$\Omega_k = 4 \left(\frac{2}{\pi}\right)^{d-1} \Pi_k \sqrt{1 - \xi^2} \quad (19)$$

$$2\gamma_k^d \int_0^1 \Omega_k(\pi\xi)^{d-1} d\xi = 1 \quad (20)$$

$$\Omega_k \sim \gamma_k^{1/2} \mathcal{V}_k^\alpha (1 - \xi)^{1/2}, \quad 1 - \xi \ll 1 \quad (21)$$

where we recall that Ω_k , γ_k and Π_k are the dimensionless fracture opening, fracture half-length ($d = 1$) or fracture radius ($d = 2$), and net pressure. We show the detailed expressions of these zero-viscosity solutions (K -vertex solutions) for plane-strain and radial hydraulic fractures in Table. 3. By setting $\alpha = 0$, we recover the zero-viscosity solutions for velocity-independent fracture toughness (Savitski and Detournay, 2002; Garagash, 2006b).

	K	$K^{[V]}$
γ_k	$\left(\frac{k}{\sqrt{2}\pi^{d-1}} \left(\frac{\alpha + d + 1/2}{\alpha + 1} \right)^\alpha \right)^{1/(\alpha+d+1/2)}$	$\left(\frac{k}{\sqrt{2}\pi^{d-1}} \left(\frac{\alpha + d + 1/2}{\alpha} \right)^\alpha \right)^{1/(\alpha+d+1/2)}$
$\frac{\Omega_k}{\sqrt{1-\xi^2}}$	$\frac{k\pi}{2} \left(\frac{\sqrt{2}}{k\pi^{\alpha+3/2}} \left(\frac{\alpha + 1}{\alpha + d + 1/2} \right)^\alpha \right)^{d/(\alpha+d+1/2)}$	$\frac{k\pi}{2} \left(\frac{\sqrt{2}}{k\pi^{\alpha+3/2}} \left(\frac{\alpha}{\alpha + d + 1/2} \right)^\alpha \right)^{d/(\alpha+d+1/2)}$
Π_k	$\frac{1}{2} \left(\frac{k^{\alpha-1/2}\pi^{d^2-1}}{2^{(d+1)(\alpha+d)}} \left(\frac{\alpha + 1}{\alpha + d + 1/2} \right)^{\alpha(d+1)} \right)^{1/(\alpha+d+1/2)}$	$\frac{1}{2} \left(\frac{k^{\alpha-1/2}\pi^{d^2-1}}{2^{(d+1)(\alpha+d)}} \left(\frac{\alpha}{\alpha + d + 1/2} \right)^{\alpha(d+1)} \right)^{1/(\alpha+d+1/2)}$

Table 3: Zero-viscosity solutions for a plane-strain ($d = 1$) and radial ($d = 2$) hydraulic fracture under the assumption of power-law velocity-dependent apparent toughness. The coefficient k is a function of the geometry parameter: $k(d = 1) = 4/\pi$ for a plane-strain fracture, and $k(d = 2) = 3$ for a radial fracture. K represents that solutions are obtained under a constant-rate fluid injection, while $K^{[V]}$ represents that solutions are obtained under a finite volume pulse.

4.3. Possible power-law exponent range suggested by scaling analysis

Assuming a constant injection rate, we have respectively $\mathcal{K} \sim t^{-1/3\alpha}$ (plane-strain) and $\mathcal{K} \sim t^{(1-5\alpha)/9}$ (radial) for different geometries. When $\alpha > 0$ (plane-strain) and $\alpha > 1/5$ (radial), the dimensionless toughness \mathcal{K} decreases with time and less energy is dissipated by the fracture surface creation compared to the viscous fluid flow. As a result, the fracture growth transitions to zero-toughness solutions at large time. However, such fracture growth has never been reported in hydraulic fracturing to the best of the authors' knowledge: this implies an upper limit of the power-law exponent- $\alpha \leq 1/5$ for most materials in hydraulic fracturing. The increase of the energy dissipation by fracture surface creation due to the increasing fracture perimeter is thus partially compensated by the decrease of the apparent fracture toughness for a radial fracture. The dimensionless toughness \mathcal{K} will increase with time and zero-viscosity solutions govern the radial hydraulic fracture growth at large time.

5. Numerical algorithm

We adopt the same numerical method as in Liu et al. (2019) and present the discretization in Appendix A.

By combining the Gauss-Chebyshev (G-C) quadrature and barycentric interpolation techniques, we turn the coupled hydraulic fracturing problem into a series of ordinary differential equations (ODEs). Solving such an ODE system calls for an initial solution of a propagating hydraulic fracture at $t = t_*$, where t_* is defined as the time when the fracture velocity becomes v_* . For a radial hydraulic fracture, the fracture growth at early time is dominated by the fluid viscosity due to the small perimeter of the fracture front: any change in the fracture toughness will have a negligible influence on fracture propagation. It is therefore reasonable to approximate the fracture propagation with zero-toughness solutions at $t < t_*$ even though the instant rate-dependent apparent toughness could be very high. For a plane-strain hydraulic fracture, we approximate the initial solutions of the solver using a self-similar solution characterized by a constant dimensionless toughness associated with K_* . Under the assumption of a constant injection rate, the fracture propagates with a larger apparent toughness prior to $t = t_*$ due to a relatively larger velocity from Eq. (1). As a result, more energy is probably dissipated by fracture surface creation before $t = t_*$. Here, we try to avoid this by selecting the reference time small enough so that the fracture growth at $t < t_*$ can be approximated by constant toughness solutions.

We also compare our numerical results with those obtained from a modified numerical solver that implements displacement discontinuity (DD) method in a length-controlled algorithm by Lu et al. (2020). Modifications are made to eliminate the wellbore and compressibility effects in the original model in Lu et al. (2020) to make the two solvers more comparable.

6. Results and discussions

We present the effect of velocity-dependent apparent toughness on the growth of hydraulic fractures by taking the values of $0 \leq \alpha < 1/5$ in the following. We choose different power-law exponents trying to cover both weak ($\alpha = 1/60$) and strong ($\alpha = 1/10$) velocity dependence.

6.1. Results for velocity-dependent fracture toughness

In this section, we assume a constant injection rate Q_o without accounting for the shut-in of fluid injection.

For a radial fracture, numerical solutions consist well with the derived scaling relations and they all converge to the zero-viscosity solutions (K in Table. 3) at large time (Fig. 1). A larger value of the power-law exponent α results in a later M - K transition as predicted by the time scale $t_{mk}(\alpha)$ definition in Eq. (17). When comparing such velocity-dependent fracture growth with constant toughness solutions using $K_{Ic} = K_*$, we find that velocity-dependent fracture growth presents a larger fracture radius, a smaller opening, and lower net pressure. A larger α power exponent characterizes a more significant difference. For the same $\alpha > 0$, the pressure gradient in the fracture becomes smaller with time (Fig. 2) and corresponds to a smaller portion of energy dissipation in the viscous fluid flow.

For a plane-strain fracture, as the toughness decreases with time during fracture propagation, a larger portion of the energy is dissipated in the viscous fluid flow. The fluid pressure gradient thus becomes larger with time and approaches to zero-toughness solutions (Fig. 2). We compare the velocity-dependent solutions with that of constant toughness K_* in Fig. 3. Similar to the radial case, we obtain a larger fracture length, and a smaller fracture opening and net pressure. A larger α leads to a faster transition to the viscosity dominated (M -) regime at large time.

We show in Figs. 1 and 3 that the results of two numerical solvers agree well except at very early time: the DD method models the fracture initiation by imposing a static initial crack, and allowing the fracture velocity first rising from zero and then decreasing with time, while the G-C method assumes a continuous propagation from the beginning. Therefore, it is expected that there would exist some discrepancy between the two solutions at early stage due to different initial conditions. However, velocity-dependent effects are very limited at this period and only become important for long-term injection/propagation. The effect of the early-time propagation history diminishes very fast with time and can be further minimized by choosing a relatively small time scale t_* compared to the interested injection duration.

We now redefine the dimensionless toughness by using the instant value of toughness $K_*(\dot{\ell}/v_*)^\alpha$

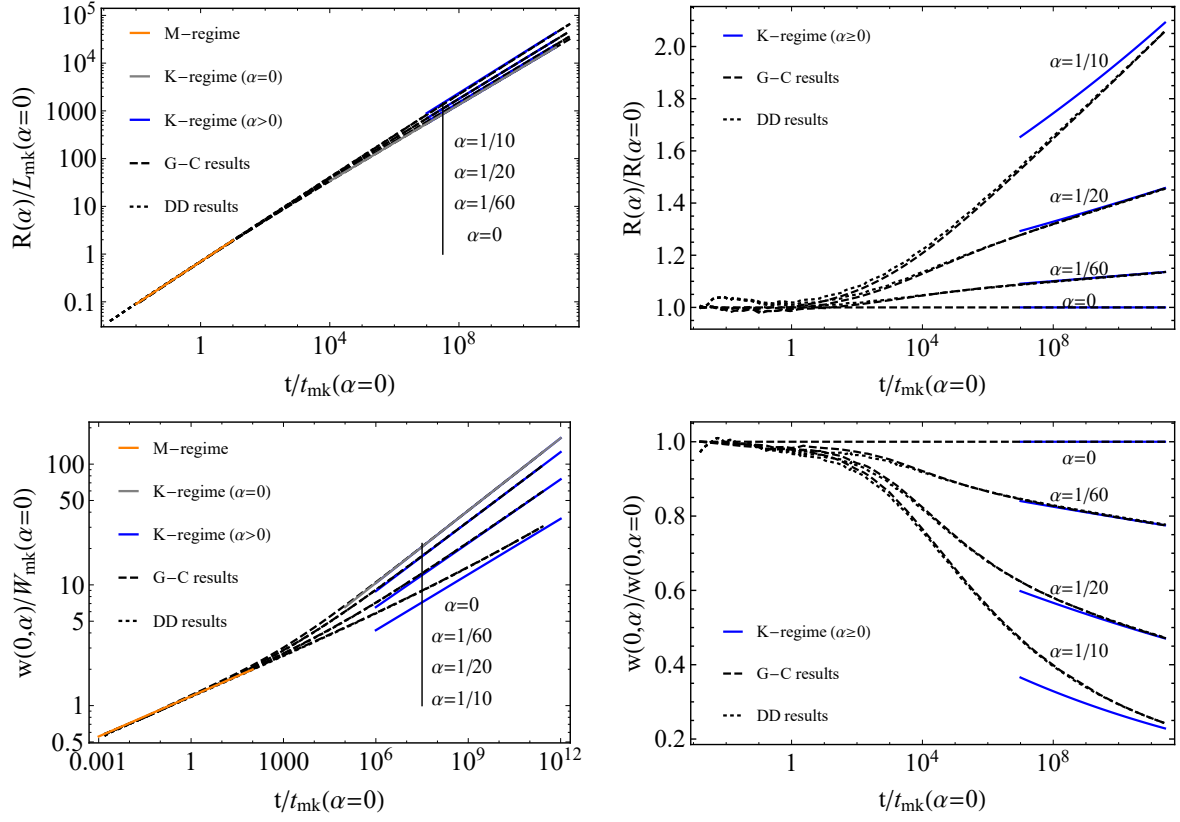


Fig. 1: Evolution of the fracture radius and fracture maximum opening in a radial fracture and their comparison with constant toughness solutions.

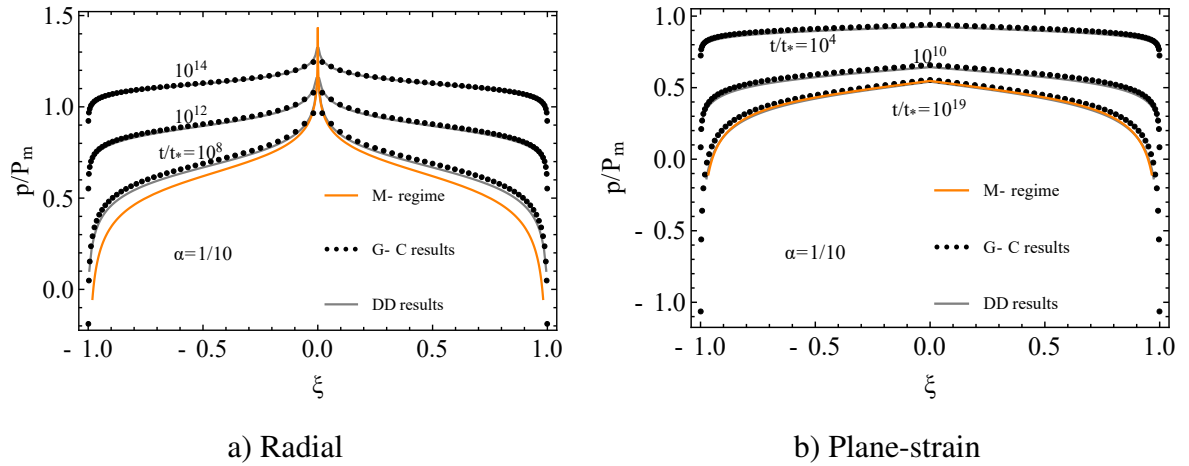


Fig. 2: Dimensionless net pressure profiles of a) a radial and b) a plane-strain fluid-driven fracture for velocity-dependent apparent toughness.

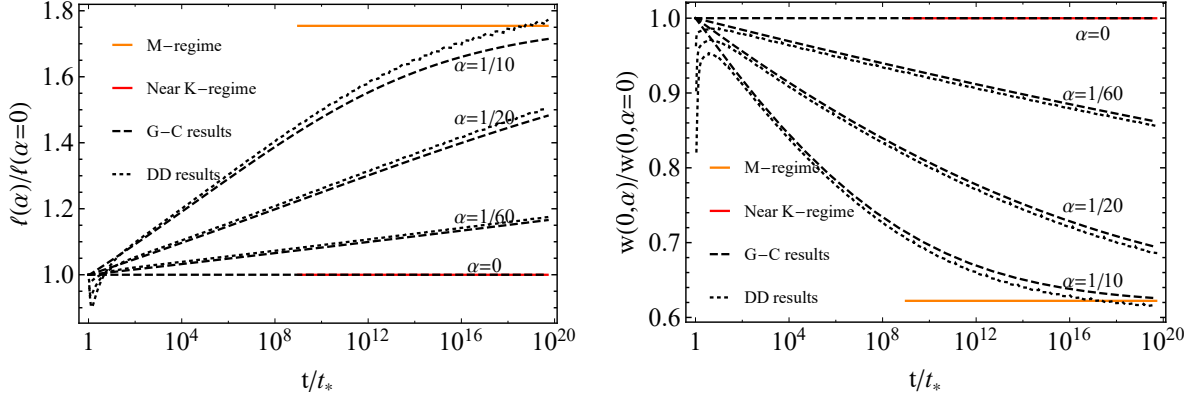


Fig. 3: Difference evolution of the fracture length and the inlet fracture opening of a plane-strain fracture compared with constant toughness solutions.

as function of the instant fracture velocity:

$$\text{Plane-strain : } \bar{\mathcal{K}}_1 = \frac{K'}{E'} \left(\frac{E'}{\mu' Q_o} \right)^{1/4} \left(\frac{\dot{\ell}}{v_*} \right)^\alpha, \quad \text{Radial : } \bar{\mathcal{K}}_2 = \frac{K'}{E'} \left(\frac{E'^5 t^2}{\mu'^5 Q_o^3} \right)^{1/18} \left(\frac{\dot{\ell}}{v_*} \right)^\alpha \quad (22)$$

Such a definition explicitly embeds the fracture velocity dependence of the fracture toughness in the same dimensionless parameter as the velocity-independent toughness case (Garagash, 2000). After re-scaling the numerical results using the viscosity scaling and this instant dimensionless toughness, the evolution of dimensionless fracture length at large time can be written as follows:

$$\text{Plane-strain : } \gamma_m \approx 0.61524; \quad \text{Radial : } \gamma_m \approx \left(\frac{3}{\pi \sqrt{2} \bar{\mathcal{K}}_2} \right)^{2/5} \quad (23)$$

As shown in Fig. 4, the dimensionless solution for any value of α expressed as a function of $\bar{\mathcal{K}}_d$ approximately collapses on the same curve as the solution for velocity-independent toughness. This implies a roughly good approximation of the fracture growth by constant toughness solutions when using an instantaneous dimensionless toughness.

6.2. Effect of a finite apparent fracture toughness below a given velocity

In the context of constant-rate fluid injection, the apparent toughness decreases with time due to a decreasing fracture velocity. However, apparent toughness does not drop to zero but stays constant once reaching its lower limit K_{\min} . Previous studies (Atkinson and Meredith, 1987; Olson, 1993) points out that the value of K_{\min} is around one tenth of the critical toughness obtained from

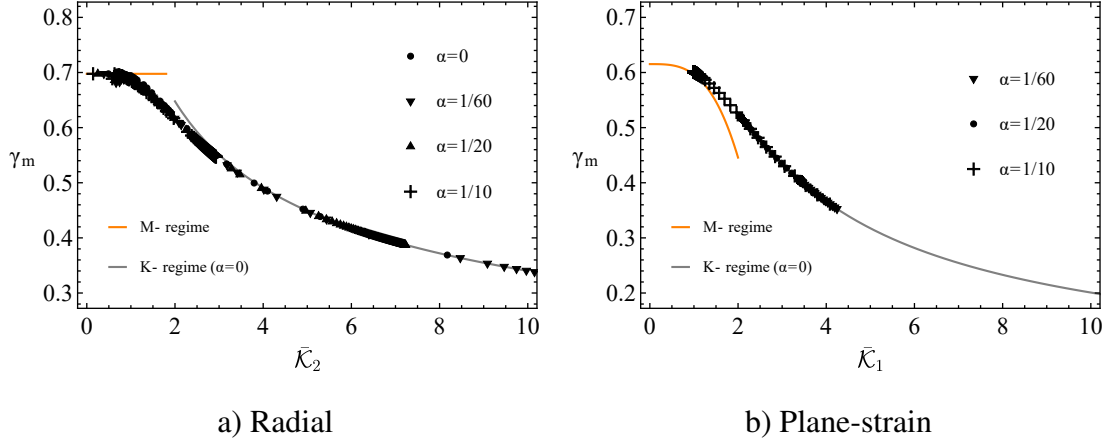


Fig. 4: Dependence of the dimensionless a) fracture radius and b) fracture half-length in the viscosity scaling on the velocity-related dimensionless toughness \bar{K}_d .

most laboratory toughness characterization. In this paper, the critical toughness is not necessarily equal to K_* since the pair of K_* and v_* are determined correspondingly to characterize the power law relation Eq. (1). It is thus reasonable to assume $1/10 \leq K_{\min}/K_* \leq 1$.

We model this lower limit of the apparent toughness as follows:

$$K_{\text{Ic}} = K_* \left(\dot{\ell}/v_* \right)^\alpha (1 - f(\dot{\ell}/v_* - r^{1/\alpha})) + K_{\min} f(\dot{\ell}/v_* - r^{1/\alpha}), \quad r = K_{\min}/K_* \quad (24)$$

Here f is a smoothed Heaviside step function $f(m) = 1/(1 + \exp(-2hm))$, where h is a positive dimensionless number controlling the smoothing of the approximation (a smaller value entails a "smoother step" - we have used $h = 130$ here).

As illustrated in Fig. 5 (for the same α but different values of K_{\min}), the hydraulic fracture evolves by first following the solution obtained previously for the power-law velocity-dependent toughness and then transitioning to the velocity-independent toughness solution at $K_{\text{Ic}} = K_{\min}$. Such a transition is nearly instantaneous for the plane-strain hydraulic fracture but can take much more time for a radial fracture since the fracturing energy results from both the fracture perimeter dimension and the apparent toughness.

6.3. Post shut-in fracture growth

The post-shut-in fracture growth has been relatively well understood for the case of constant toughness (Garagash, 2006a; Möri and Lecampion, 2021). When toughness dominates the fracture

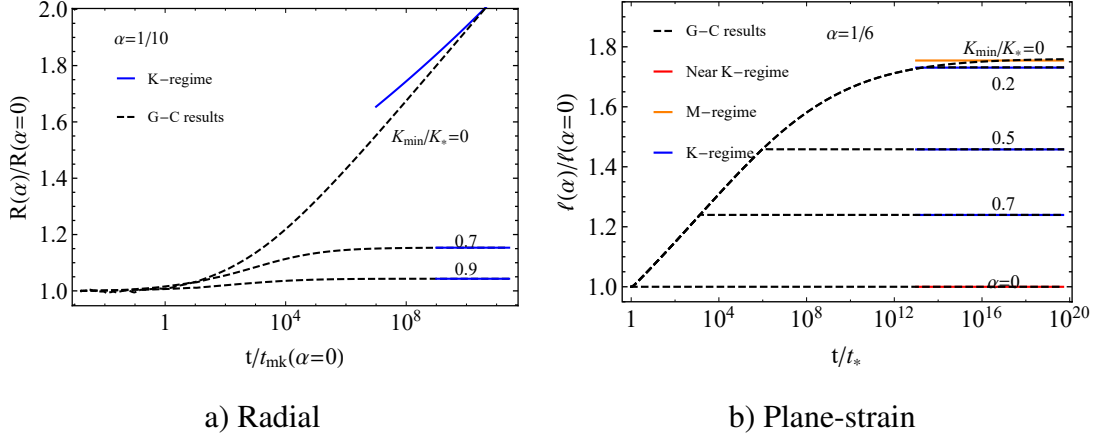


Fig. 5: Difference evolution of the a) fracture radius and b) fracture half-length with different lower limits of the apparent toughness.

growth, the fracture immediately arrests upon stop of fluid injection. Otherwise, the fracture continues to propagate until viscous forces become negligible in the fluid flow. However, for velocity-dependent apparent toughness, the fracture growth rate after shut-in further decreases compared with the propagation phase. It leads to a more significant drop in the apparent fracture toughness which deviates the fracture behavior from constant toughness predictions. Accounting for such velocity-dependent effects, we investigate in the following the scaling relations of different fracture growth regimes after the shut-in. We also compare our (semi-)analytical estimates/solutions with the numerical simulation.

We introduce V_s as the finite pulse. It equals $V_s = Q_o t_s$ when assuming a constant injection rate Q_o prior to the shut-in $t = t_s$. Following the same procedure as in Section 4, we obtain two scaling relations ($M^{[V]}$ - and $K^{[V]}$ -scaling as shown in Table. 2) with which we set $\alpha = 0$ and recover the constant toughness scaling relations (Garagash, 2006a; Möri and Lecampion, 2021).

The pulse-viscosity $M^{[V]}$ -regime represents that the fluid viscosity dominates the fracture propagation after shut-in. In the limit of zero toughness, the fracture problem becomes self-similar and can be solved numerically using the G-C method. The solution for a radial fracture is available in literature (Möri and Lecampion, 2021) with the dimensionless fracture radius of $\gamma_m^{[V]} = 0.8360$ expressed in the $M^{[V]}$ -scaling. We thus only solve the self-similar problem for the plane-strain geometry and obtain a dimensionless fracture half-length of $\gamma_m^{[V]} = 0.8026$ (see more details in

Appendix B).

The pulse-toughness $K^{[V]}$ regime indicates that toughness dominates the fracture growth after shut-in. Different from constant toughness solutions, the fracture continues to propagate after shut-in even when viscous forces are negligible in the fluid flow. Assuming uniform pressure inside the fracture, we obtain the pulse-toughness solutions ($K^{[V]}$ in Table. 3).

A time scale $t_{mk}^{[V]}$ characterizes the transition between the $M^{[V]}$ - and $K^{[V]}$ - regime. A dimensionless toughness $\mathcal{K}^{[V]}$ which is a function of the transition time scale describes the evolution of toughness-viscosity energy dissipation ratio after shut-in:

$$\mathcal{K}^{[V]} = \left(\frac{t}{t_{mk}^{[V]}} \right)^{(1+2d-4\alpha-6\alpha d)/(6(d+1))} = \mathcal{K}_s \left(\frac{t}{t_s} \right)^{(1+2d-4\alpha-6\alpha d)/(6(d+1))}, \quad t_{mk}^{[V]} = \left(\frac{t_{mk}^{2\alpha-6\alpha d+2d-2}}{t_s^{6\alpha-3}} \right)^{1/(-4\alpha-6\alpha d+2d+1)} \quad (25)$$

where $\mathcal{K}_s = \mathcal{K}(t = t_s)$ is the dimensionless toughness (as defined in Eq. (17)) at the shut-in time $t = t_s$. When $\alpha > 0.3$ (plane-strain) and $\alpha > 0.325$ (radial), the dimensionless toughness $\mathcal{K}^{[V]}$ decreases with time. The fracture grows without arrest and viscous fluid flow always dominates the energy dissipation. This however goes against our assumption of $0 \leq \alpha < 1/5$. We thus focus on the shut-in cases with $\alpha < 1/5 < 0.3$ (plane-strain) and $\alpha < 1/5 < 0.325$ (radial) in what follows.

For $\alpha < 1/5$, $\mathcal{K}^{[V]}$ increases with time and the hydraulic fracture growth always transitions to the pulse-toughness solutions at large time. However, the detailed changes of the post-shut-in propagation depends on the dimensionless toughness at the shut-in \mathcal{K}_s as shown in Figs. 6 and 7. For $\mathcal{K}_s \ll 1$, the fluid viscosity dominates the fracture growth upon shut-in, the solution transitions from constant injection rate viscosity dominated (M -) regime towards the pulse-viscosity $M^{[V]}$ solutions. Such a transition is however missing for $\mathcal{K}_s \gg 1$: the fracture toughness dominates the fracture growth at shut-in and the fracture immediately transitions from the constant injection rate toughness dominated (K -) regime to the pulse-toughness $K^{[V]}$ solution.

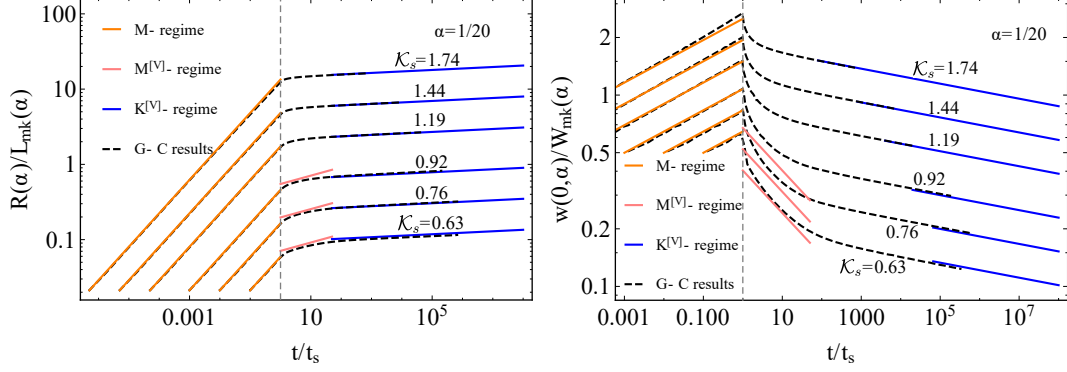


Fig. 6: Evolution of the fracture radius and inlet fracture opening for a radial hydraulic fracture with different dimensionless toughness at the shut-in \mathcal{K}_s . The vertical dashed line indicates the shut-in time. The pulse-viscosity $M^{[V]}$ solutions (Möri and Lecampion, 2021) are shown in pink and are unlikely to reach during the transition process when $\mathcal{K}_s > 1$. We therefore do not show these solutions for $\mathcal{K}_s > 1$.

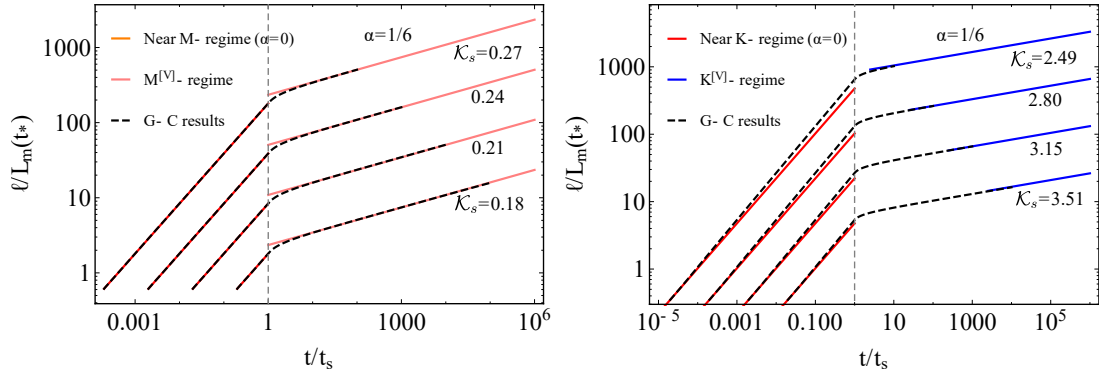


Fig. 7: Evolution of the fracture half-length for a plane-strain hydraulic fracture with different dimensionless toughness at the shut-in \mathcal{K}_s . The vertical dashed line indicates the shut-in time. The transition towards the pulse-viscosity $M^{[V]}$ solutions (in pink) only occurs when $\mathcal{K}_s \ll 1$. We therefore do not show the $M^{[V]}$ solutions for $\mathcal{K}_s > 1$.

6.4. Fracture arrest

When accounting for a lower limit of the apparent toughness K_{\min} , the fracture propagation finally arrests with a uniquely defined fracture extent.

$$R_a = \left(\frac{k}{\sqrt{2}\pi^{d-1}} \frac{E' V_s}{K' r} \right)^{1/(d+1/2)} \quad (26)$$

where the subscript a represents the arrest of the propagation, and $r = K_{\min}/K_*$ the ratio between the minimum value of the apparent toughness and the reference toughness K_* . The coefficient k is a function of the fracture geometry: $k(d = 1) = 4/\pi$ for a plane-strain fracture, and $k(d = 2) = 3$ for the radial geometry. When comparing with the arrest fracture size with that of a constant fracture toughness, we have

$$R_a(\alpha)/R_a(\alpha = 0) = (1/r)^{1/(d+1/2)} \quad (27)$$

Taking $r = 1/10$, we have $R_a(\alpha)/R_a(\alpha = 0) \approx 2.51$ for a radial fracture, and $R_a(\alpha)/R_a(\alpha = 0) \approx 4.64$ for a plane-strain fracture. We further quantify this arrest fracture extent in Table. 4 using values for material and injection parameters representative of an industrial fracturing treatment and a geological dike growth (Möri and Lecampion, 2021). This rate-dependent apparent toughness adds a significant amount of fracture extension compared to the case of constant fracture toughness. However, one needs to be careful with such a conclusion since the leak-off, which has been neglected in this study, will likely make the arrest occur earlier. Our results thus correspond to an upper limit of the fracture arrest extension.

The arrest time t_a however results from both the velocity dependence of the apparent toughness and the shut-in time t_s . When the lower bound toughness is reached before the shut-in, the fracture growth transitions to the constant-toughness solution. It arrests immediately at the shut-in time $t_a = t_s$ only when the transition to the constant toughness solution finishes before the shut-in ($t_{mk}(\alpha) \ll t_s$). Otherwise, the hydraulic fracture will continue to grow for a finite duration either with its apparent toughness further decreasing to the minimum K_{\min} or with the pressure gradient inside the fracture dropping to zero.

Cases	$R_a(\alpha = 0)$	$R_a(\alpha, r = 4/5)$	$R_a(\alpha, r = 1/2)$	$R_a(\alpha, r = 1/10)$
Slickwater injection into a mudstone	56 m	61 m	74 m	141 m
Magma injection	4.64 km	5.07 km	6.12 km	11.66 km

Table 4: Arrest fracture radius R_a with different values of $r = K_{\min}/K_*$ for industrial hydraulic fracture injections ($\mu = 1 \text{ Pa} \cdot \text{s}$, $V_s = 27 \text{ m}^3$, $E' = 30/(1 - 0.25^2) \text{ GPa}$, $K_* = 1 \text{ MPa} \cdot \text{m}^{1/2}$) and a magma release ($\mu = 200 \text{ Pa} \cdot \text{s}$, $V_s = 5 \times 10^5 \text{ m}^3$, $E' = 20/(1 - 0.2^2) \text{ GPa}$, $K_* = 1.5 \text{ MPa} \cdot \text{m}^{1/2}$). We neglect buoyant forces and assume a Newtonian rheology for the magma of the dike.

6.5. Propagation regime diagram

We summarize the effects of power-law velocity-dependent fracture toughness on the pre- and post-shut-in growth of a hydraulic fracture in Fig. 8. We illustrate how the shut-in time t_s influences the regime transition paths.

The propagation path starts at a point located on the M - K edge for a plane-strain fracture, which represents the energy dissipation in fracture surface creation over that in viscous fluid flow. This starting point becomes the M -vertex for a radial fracture, which results from the negligible energy dissipation associated with fracture surface creation due to the small fracture geometry. As the fracture extends, the apparent toughness of both geometries decreases with time and stays constant once it reaches its minimum value K_{\min} . We define the time at which the apparent toughness reaches the minimum as $t(K_{\text{Ic}} = K_{\min})$. When there is stop of fluid injection, the fracture propagation changes and depends on the dimensionless toughness at the time of shut-in \mathcal{K}_s . When viscous fluid flow dominates the propagation with $\mathcal{K}_s \ll 1$, both fracture geometries first transition towards to the pulse-viscosity solution ($M^{[V]}$ -regime) and then converges to the zero-viscosity solutions at large time. Otherwise, the fracture transitions directly to the pulse-toughness solution ($K^{[V]}$ -regime). During this stage, the post-shut-in dimensionless toughness $\mathcal{K}^{[V]}$ always increases with time while the apparent toughness decreases with time until reaching its minimum K_{\min} . When the minimum is reached before the shut-in time $t(K_{\text{Ic}} = K_{\min}) < t_s$, an immediate arrest occurs at $t = t_s$ if toughness dominates the growth ($\mathcal{K}_s \gg 1$), otherwise the fracture continues to grow but takes a shorter period to stop compared to the case of $t(K_{\text{Ic}} = K_{\min}) > t_s$. The fracture finally arrests with the toughness staying at its minimum value $K_{\text{Ic}} = K_{\min}$ and viscous forces being

heterogeneity and does not necessarily lead to a power-law relation with respect to the instantaneous fracture velocity. In some cases, for example during the growth of a plane-strain hydraulic fracture in the viscosity-dominated regime (Da Fies et al., 2022b), the apparent toughness can be simply approximated by the maximum toughness in the heterogeneous medium (Dontsov and Suarez-Rivera, 2021).

One may also apply the methods reported in this paper to the case of a heterogeneous toughness by relating the propagation criterion/toughness to the fracture length $K_{Ic}(\ell)$. Such an extension of the methods however does not naturally favour a piece-wise toughness distribution in space and leads to limited solution accuracy at the very early stage of fracture growth. Full consideration of the fracture dynamics such as the piece-wise fracture propagation (see Cao et al., 2017; Peruzzo et al., 2019a,b, and references therein), the re-nucleation or the stopping and restarting of hydraulic fractures (which are more likely to occur in a heterogeneous medium) necessitates an algorithm to capture the fracture front velocity in a much more precise manner (Wrobel and Mishuris, 2015; Peck et al., 2018).

7. Conclusion

We investigate the effects of velocity-dependent apparent fracture toughness on hydraulic fracture propagation based on a power-law empirical model. Under such an assumption, both the plane-strain and radial fracture present decreasing toughness when the fracture extends. As a result, the plane-strain fracture evolves towards the viscosity dominated regime at large time, while the radial fracture evolves toward a regime dominated by fracture toughness. This difference results from a total increase of energy dissipation in creating fracture surfaces for the radial fracture. For both geometries, the fracture growth can be approximated by constant toughness solutions with the instantaneous toughness value. After the shut-in, the fracture grows at a much lower growth rate and transitions to a pulse-toughness solution at large time. The fracture finally arrests when apparent toughness reaches its minimum and viscous forces inside the fracture become negligible. The arrest dimension can be several times larger than constant toughness predictions when neglecting fluid leak-off to the solid. The reported fracture growth patterns before and after

the stop of fluid injection may help guide and interpret laboratory or field observation related to rate-dependent hydraulic fracture growth.

CRedit authorship contribution statement

Dong Liu: Conceptualization, Formal analysis, Investigation, Methodology, Software, Validation, Visualization, Writing - original draft; Guanyi Lu: Conceptualization, Software, Validation, Writing - review & editing.

Declaration of competing interest

The authors declare that they have no known competing financial interests or personal relationships that could have appeared to influence the work reported in this paper.

Appendix A. Discretization using the Gauss-Chebyshev quadrature

Gauss-Chebyshev quadrature combined with the Barycentric interpolation techniques provide an efficient way to solve elastic boundary integral solutions arising in fracture problems (Viesca and Garagash, 2017; Liu and Brantut, 2022). It has been recently applied to semi-infinite (Garagash, 2019) and finite hydraulic fracture propagation problems (Liu et al., 2019; Kanin et al., 2021; Möri and Lecampion, 2021; Pereira and Lecampion, 2021), illustrating a spectral accuracy and efficiency in large time span semi-analytical investigation. In this paper, following Liu et al. (2019) we use the first type Gauss-Chebyshev quadrature T_k to discretize the fracture. It consists of two sets of nodes whose values in the range of $(-1,1)$.

$$s_j = \cos\left(\frac{\pi(j-1/2)}{n}\right), j = 1, \dots, n; \quad x_i = \cos\left(\frac{\pi i}{n}\right), i = 1, \dots, n-1, \quad (\text{A.1})$$

where n is the number of unknowns. These nodes naturally include the dislocation singularity appearing at the fracture tips in linear elastic fracture mechanics.

$$\frac{dw}{ds} = \omega(s)F(s), \quad \omega(s) = \frac{1}{\sqrt{1-s^2}} \quad (\text{A.2})$$

where $F(s)$ is an non-singular unknown. Following Viesca and Garagash (2017); Liu et al. (2019), we discretize the governing equations as follows.

Elasticity.

$$\frac{4\ell}{E'} \mathbf{p} = \mathbb{G}_d \cdot \mathbf{F} \quad (\text{A.3})$$

where \mathbb{G}_d is the elasticity quadrature matrix. For a plane-strain hydraulic fracture ($d = 1$),

$$\mathbb{G}_1 = \mathbb{H} = \left\{ \frac{1}{n} \frac{1}{z_i - s_j} \right\} \quad (\text{A.4})$$

where \mathbb{H} is the Hilbert transform matrix. For a radial hydraulic fracture ($d = 2$),

$$\mathbb{G}_2 = \mathbb{H} + \frac{1}{2\mathbf{z}} \mathbb{T} \cdot \mathbb{H} + \Delta \mathbb{G} \quad (\text{A.5})$$

where $\mathbb{T} = \{T_{ii'}\}$ is the \mathbf{z} -grid integration matrix and $\Delta \mathbb{G} = \left\{ \frac{1}{n} \Delta \left(G_2(z_i, s_j) - \frac{1}{z_i - s_j} - \frac{\ln|z_i - s_j|}{2z_i} \right) \right\}$.

Lubrication flow.

$$-\frac{1}{d} \mathbf{z}^d \frac{\partial}{\partial t} (\mathbb{S} \cdot \mathbf{F}) + \frac{1}{d} \frac{\partial}{\partial t} (\mathbb{S} \cdot (\mathbf{s}^d \mathbf{F})) + \frac{\dot{\ell}}{\ell} (\mathbb{S} \cdot (\mathbf{s}^d \mathbf{F})) = -\frac{E'}{4\mu' \ell^3} (\mathbb{S} \cdot \mathbf{F})^3 \mathbf{z}^{d-1} (\mathbb{D} \cdot \mathbb{G}_d \cdot \mathbf{F}) \quad (\text{A.6})$$

Global continuity equation.

$$\mathbf{S}_A \cdot (\mathbf{s} \mathbf{F}) + \frac{V}{\ell} = 0 \text{ for plane-strain, } \mathbf{S}_H \cdot (\mathbf{s}^2 \mathbf{F}) + \frac{V}{\pi \ell^2} = 0 \text{ for radial} \quad (\text{A.7})$$

Propagation criterion.

$$\mathbf{Q} \cdot \mathbf{F} = -\frac{1}{\sqrt{2}} \frac{K'_* \ell^{1/2}}{E'} \left(\frac{\dot{\ell}}{v_*} \right)^\alpha \quad (\text{A.8})$$

\mathbb{S} , \mathbf{S}_A and \mathbf{S}_H are integration operators, \mathbf{D} is the differentiation operator and \mathbf{Q} is the extrapolation operator, see the expressions with the same notations in Liu et al. (2019) for more details.

The unknowns of these ODEs therefore become the unknown vector $\mathbf{F} = \{F(s_j)\}$, $j = 1, \dots, n$ and the fracture dimension ℓ . We use $n = 80$ for a plane-strain fracture and $n = 81$ for a radial fracture for all the simulations presented in this paper.

Appendix B. Pulse-viscosity solutions in the limit of zero toughness

For a plane-strain hydraulic fracture, we rewrite the dimensionless governing equations in the pulse-viscosity scaling $M^{[V]}$ by introducing a new dimensionless opening following Garagash and Detournay (2005).

$$\bar{\Omega}_m^{[V]} = \Omega_m^{[V]} / \gamma_m^{[V]} \quad (\text{B.1})$$

Assuming zero fracture toughness, the governing equations (12), (13), (14), (15) become:

$$4\Pi_m^{[V]} = \frac{1}{\pi} \int_{-1}^{+1} \frac{\partial \bar{\Omega}_m^{[V]}}{\partial \xi'} G_1(\xi, \xi') d\xi' \quad (\text{B.2})$$

$$\frac{1}{6} \xi \bar{\Omega}_m^{[V]} + (\bar{\Omega}_m^{[V]})^3 \frac{d\Pi}{d\xi} = 0 \quad (\text{B.3})$$

$$\int_{-1}^1 \bar{\Omega}_m^{[V]} d\xi = \frac{1}{(\gamma_m^{[V]})^2} \quad (\text{B.4})$$

$$\bar{\Omega}_m^{[V]} \sim \frac{\mathcal{K}^{[V]}}{\sqrt{\gamma_m^{[V]}}} (1 - \xi)^{1/2}, \quad \mathcal{K}^{[V]} = 0 \quad (\text{B.5})$$

We select the Gauss-Chebyshev polynomials of the first type T_n for discretization,

$$\frac{\partial \bar{\Omega}_m^{[V]}}{\partial s} = \omega(s) F(s), \quad \omega(s) = \frac{1}{\sqrt{1 - s^2}} \quad (\text{B.6})$$

We back-substitute the elasticity into the lubrication equations and obtain $(n + 1)$ discretized equations with $(n + 1)$ unknowns $\{\gamma_m^{[V]}, \mathbf{F}\}$:

$$\frac{1}{6} \mathbf{z}(\mathbb{S} \cdot \mathbf{F}) + (\mathbb{S} \cdot \mathbf{F})^3 \left(\mathbb{D} \cdot \left(\frac{1}{4} \mathbb{G}_1 \cdot \mathbf{F} \right) \right) = 0 \quad (\text{B.7})$$

$$\mathbf{S}_A \cdot (\mathbf{s} \mathbf{F}) + \frac{1}{(\gamma_m^{[V]})^2} = 0 \quad (\text{B.8})$$

$$\mathbf{Q} \cdot \mathbf{F} = 0 \quad (\text{B.9})$$

On the account of the problem symmetry, we solve the first $(n/2 - 1)$ equations of Eq. (B.7) together with Eq. (B.8) and (B.9) using the built-in Newton scheme of Mathematica. With $n = 300$ points, we obtain the dimensionless half fracture length as

$$\text{Plane-strain: } \gamma_m^{[V]} \approx 0.8026 \quad (\text{B.10})$$

We show the corresponding dimensionless pressure and width profile in Fig. B.9.

References

Albertini, G., Lebihain, M., Hild, F., Ponson, L., Kammer, D.S., 2021. Effective toughness of heterogeneous materials with rate-dependent fracture energy. *Physical Review Letters* 127, 35501.

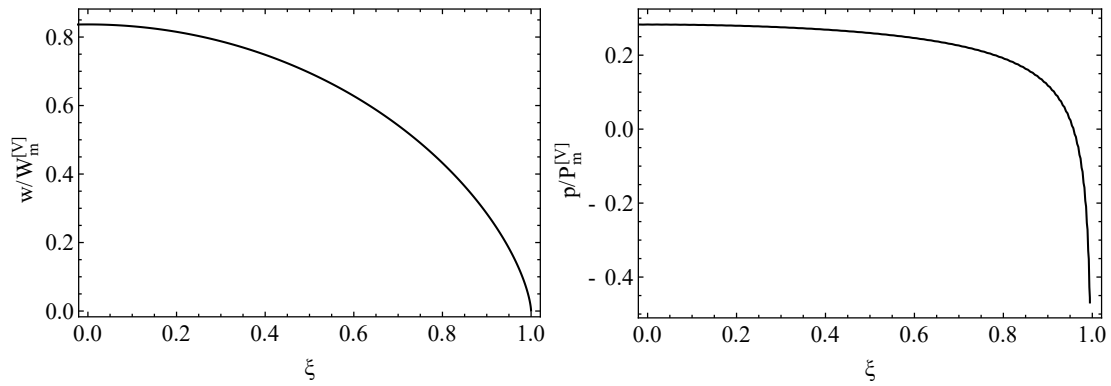


Fig. B.9: Self-similar solutions of the zero-toughness post-shut-in fracture growth for a plane-strain hydraulic fracture. $W_m^{[V]}$ and $P_m^{[V]}$ correspond to the scaling relations of the $M^{[V]}$ -regime as shown in Table. 2.

- Aliha, M.R.M., Samareh-Mousavi, S.S., Mirsayar, M.M., 2021. Loading rate effect on mixed mode I/II brittle fracture behavior of PMMA using inclined cracked SBB specimen. *International Journal of Solids and Structures* 232, 111177.
- Anderson, T.L., 2017. *Fracture mechanics: fundamentals and applications*. CRC press.
- Atkins, A.G., Lee, C., Caddell, R.M., 1975. Time-temperature dependent fracture toughness of PMMA. *Journal of Materials Science* 10, 1381–1393.
- Atkinson, B.K., 1984. Subcritical crack growth in geological materials. *Journal of Geophysical Research: Solid Earth* 89, 4077–4114.
- Atkinson, B.K., Meredith, P.G., 1987. Experimental fracture mechanics data for rocks and minerals. *Fracture Mechanics of Rock*, 477.
- Batchelor, G.K., 2000. *An introduction to fluid dynamics*. Cambridge university press.
- Baumberger, T., Caroli, C., Martina, D., 2006. Solvent control of crack dynamics in a reversible hydrogel. *Nature Materials* 5, 552–555.
- Bažant, Z.P., Gettu, R., 1992. Rate effects and load relaxation in static fracture of concrete. *ACI Materials Journal* 89, 456–468.
- Bertram, A., Kalthoff, J., 2003. Crack propagation toughness of rock for the range of low to very high crack speeds. *Key Engineering Materials* 251, 423–430.
- Brantut, N., Heap, M.J., Meredith, P.G., Baud, P., 2013. Time-dependent cracking and brittle creep in crustal rocks: A review. *Journal of Structural Geology* 52, 17–43.
- Cao, T.D., Milanese, E., Remij, E.W., Rizzato, P., Remmers, J.J., Simoni, L., Huyghe, J.M., Hussain, F., Schrefler, B.A., 2017. Interaction between crack tip advancement and fluid flow in fracturing saturated porous media. *Mechanics Research Communications* 80, 24–37.
- Charles, R., 1958. Static fatigue of glass. I. *Journal of Applied Physics* 29, 1549–1553.

- Chen, L., Zhang, G., Zou, Z., Guo, Y., Zheng, X., 2021. The effect of fracture growth rate on fracture process zone development in quasi-brittle rock. *Engineering Fracture Mechanics* 258, 108086.
- Cleary, M.P., Wong, S.K., 1985. Numerical simulation of unsteady fluid flow and propagation of a circular hydraulic fracture. *International Journal for Numerical and Analytical Methods in Geomechanics* 9, 1–14.
- Da Fies, G., 2020. Effective time-space adaptive algorithm for hydraulic fracturing. Ph.D. thesis. Aberystwyth University.
- Da Fies, G., Dutko, M., Mishuris, G., 2021. Remarks on dealing with toughness heterogeneity in modelling of hydraulic fracture, in: 55th US Rock Mechanics/Geomechanics Symposium, OnePetro.
- Da Fies, G., Dutko, M., Peck, D., 2022a. Averaging-based approach to toughness homogenisation for radial hydraulic fracture. *arXiv preprint arXiv:2211.03114*.
- Da Fies, G., Peck, D., Dutko, M., Mishuris, G., 2022b. A temporal averaging-based approach to toughness homogenisation in heterogeneous material. *Mathematics and Mechanics of Solids*, 1081286522117553.
- Dai, F., Xia, K.W., 2013. Laboratory measurements of the rate dependence of the fracture toughness anisotropy of Barre granite. *International Journal of Rock Mechanics and Mining Sciences* 60, 57–65.
- Darot, M., Gueguen, Y., 1986. Slow crack growth in minerals and rocks: Theory and experiments. *Pure and Applied Geophysics* 124, 677–692.
- Detournay, E., 2004. Propagation regimes of fluid-driven fractures in impermeable rocks. *International Journal of Geomechanics* 4, 35–45.
- Detournay, E., Peirce, A.P., 2014. On the moving boundary conditions for a hydraulic fracture. *International Journal of Engineering Science* 84, 147–155.
- Dontsov, E., Suarez-Rivera, R., 2021. Representation of high resolution rock properties on a coarser grid for hydraulic fracture modeling. *Journal of Petroleum Science and Engineering* 198, 108144.
- Ernesti, F., Schneider, M., 2022. Computing the effective crack energy of heterogeneous and anisotropic microstructures via anisotropic minimal surfaces. *Computational Mechanics* 69, 45–57.
- Freiman, S., 1984. Effects of chemical environments on slow crack growth in glasses and ceramics. *Journal of Geophysical Research: Solid Earth* 89, 4072–4076.
- Gao, G., Yao, W., Xia, K., Li, Z., 2015. Investigation of the rate dependence of fracture propagation in rocks using digital image correlation (DIC) method. *Engineering Fracture Mechanics* 138, 146–155.
- Garagash, D.I., 2000. Hydraulic fracture propagation in elastic rock with large toughness, in: 4th North American Rock Mechanics Symposium, American Rock Mechanics Association. pp. 221–228.
- Garagash, D.I., 2006a. Plane-strain propagation of a fluid-driven fracture during injection and shut-in: Asymptotics of large toughness. *Engineering fracture mechanics* 73, 456–481.
- Garagash, D.I., 2006b. Propagation of a plane-strain hydraulic fracture with a fluid lag: Early-time solution. *International Journal of Solids and Structures* 43, 5811–5835.

- Garagash, D.I., 2019. Cohesive-zone effects in hydraulic fracture propagation. *Journal of the Mechanics and Physics of Solids* 133, 103727.
- Garagash, D.I., Detournay, E., 2005. Plane-strain propagation of a fluid-driven fracture: small toughness solution. *Journal of applied mechanics* 72, 916–928.
- Goldman, T., Livne, A., Fineberg, J., 2010. Acquisition of inertia by a moving crack. *Physical Review Letters* 104, 114301.
- Gordeliy, E., Detournay, E., 2011. A fixed grid algorithm for simulating the propagation of a shallow hydraulic fracture with a fluid lag. *International Journal for Numerical and Analytical Methods in Geomechanics* 35, 602–629.
- Hills, D.A., Kelly, P.A., Dai, D.N., Korsunsky, A.M., 2013. *Solution of crack problems: the distributed dislocation technique*. volume 44. Springer Science & Business Media.
- Hossain, M., Hsueh, C.J., Bourdin, B., Bhattacharya, K., 2014. Effective toughness of heterogeneous media. *Journal of the Mechanics and Physics of Solids* 71, 15–32.
- Kanin, E., Dontsov, E., Garagash, D., Osipov, A., 2021. A radial hydraulic fracture driven by a herschel–bulkley fluid. *Journal of Non-Newtonian Fluid Mechanics* 295, 104620.
- Kwon, H.J., Rogalsky, A.D., Kim, D.W., 2011. On the measurement of fracture toughness of soft biogel. *Polymer Engineering & Science* 51, 1078–1086.
- Lawn, B.R., 1993. *Fracture of brittle solids*. Cambridge University Press.
- Lebihain, M., Leblond, J.B., Ponson, L., 2020. Effective toughness of periodic heterogeneous materials: the effect of out-of-plane excursions of cracks. *Journal of the Mechanics and Physics of Solids* 137, 103876.
- Lebihain, M., Ponson, L., Kondo, D., Leblond, J.B., 2021. Effective toughness of disordered brittle solids: A homogenization framework. *Journal of the Mechanics and Physics of Solids* 153, 104463.
- Liu, D., Brantut, N., 2022. Micromechanical controls on the brittle-plastic transition in rocks. *arXiv preprint arXiv:2211.11831*.
- Liu, D., Lecampion, B., 2022. Laboratory investigation of hydraulic fracture growth in zimbabwe gabbro. *Journal of Geophysical Research-Solid Earth* 127, e2022JB025678.
- Liu, D., Lecampion, B., 2023. Measurements of the evolution of the fluid lag in laboratory hydraulic fracture experiments in rocks. *Mechanics of Hydraulic Fracturing: Experiment, Model, and Monitoring*, 11–23.
- Liu, D., Lecampion, B., Blum, T., 2020. Time-lapse reconstruction of the fracture front from diffracted waves arrivals in laboratory hydraulic fracture experiments. *Geophysical Journal International* 223, 180–196.
- Liu, D., Lecampion, B., Garagash, D.I., 2019. Propagation of a fluid-driven fracture with fracture length dependent apparent toughness. *Engineering Fracture Mechanics* 220, 106616.
- Lu, G., Gordeliy, E., Prioul, R., Aidagulov, G., Uwaifo, E.C., Ou, Q., Bunger, A.P., 2020. Time-dependent hydraulic fracture initiation. *Journal of Geophysical Research: Solid Earth* 125, e2019JB018797.
- Lu, G., Gordeliy, E., Prioul, R., Bunger, A., 2017. Modeling initiation and propagation of a hydraulic fracture under

- subcritical conditions. *Computer Methods in Applied Mechanics and Engineering* 318, 61–91.
- Mahanta, B., Tripathy, A., Vishal, V., Singh, T.N., Ranjith, P.G., 2017. Effects of strain rate on fracture toughness and energy release rate of gas shales. *Engineering Geology* 218, 39–49.
- Möri, A., Lecampion, B., 2021. Arrest of a radial hydraulic fracture upon shut-in of the injection. *International Journal of Solids and Structures* 219, 151–165.
- Oh, S.W., Min, G.J., Park, S.W., Kim, M.S., Obara, Y., Cho, S.H., 2019. Anisotropic influence of fracture toughness on loading rate dependency for granitic rocks. *Engineering Fracture Mechanics* 221, 106677.
- Olson, J.E., 1993. Joint pattern development: Effects of subcritical crack growth and mechanical crack interaction. *Journal of Geophysical Research: Solid Earth* 98, 12251–12265.
- Olson, J.E., 2004. Predicting fracture swarms—the influence of subcritical crack growth and the crack-tip process zone on joint spacing in rock. *Geological Society, London, Special Publications* 231, 73–88.
- Olson, J.E., Taleghani, A.D., 2009. Modeling simultaneous growth of multiple hydraulic fractures and their interaction with natural fractures, in: *SPE hydraulic fracturing technology conference*, OnePetro. p. 119739.
- Peck, D., Wrobel, M., Perkowska, M., Mishuris, G., 2018. Fluid velocity based simulation of hydraulic fracture: a penny shaped model—part i: the numerical algorithm. *Meccanica* 53, 3615–3635.
- Peirce, A., 2022. The arrest and recession dynamics of a deflating radial hydraulic fracture in a permeable elastic medium. *Journal of the Mechanics and Physics of Solids* , 104926.
- Peirce, A., Detournay, E., 2022a. The arrest and recession dynamics of a deflating hydraulic fracture in a permeable elastic medium in a state of plane strain. *International Journal of Solids and Structures* , 111906.
- Peirce, A., Detournay, E., 2022b. Sunset similarity solution for a receding hydraulic fracture. *Journal of Fluid Mechanics* 944.
- Pereira, L., Lecampion, B., 2021. A plane-strain hydraulic fracture driven by a shear-thinning carreau fluid. *International Journal for Numerical and Analytical Methods in Geomechanics* 45, 1603–1623.
- Peruzzo, C., Cao, D., Milanese, E., Favia, P., Pesavento, F., Hussain, F., Schrefler, B.A., 2019a. Dynamics of fracturing saturated porous media and self-organization of rupture. *European Journal of Mechanics-A/Solids* 74, 471–484.
- Peruzzo, C., Simoni, L., Schrefler, B., 2019b. On stepwise advancement of fractures and pressure oscillations in saturated porous media. *Engineering Fracture Mechanics* 215, 246–250.
- Pohlit, D.J., Dillard, D.A., Jacob, G.C., Starbuck, J.M., 2008. Evaluating the rate-dependent fracture toughness of an automotive adhesive. *The Journal of Adhesion* 84, 143–163.
- Ponson, L., 2009. Depinning transition in the failure of inhomogeneous brittle materials. *Physical Review Letters* 103, 55501.
- Rice, J.R., 1968. Mathematical analysis in the mechanics of fracture. *Fracture: an advanced treatise* 2, 191–311.
- Rosakis, A.J., Zehnder, A.T., 1985. On the dynamic fracture of structural metals. *International Journal of Fracture* 27, 169–186.

- Savitski, A.A., Detournay, E., 2002. Propagation of a penny-shaped fluid-driven fracture in an impermeable rock: asymptotic solutions. *International Journal of Solids and Structures* 39, 6311–6337.
- Scheibert, J., Guerra, C., Célarié, F., Dalmas, D., Bonamy, D., 2010. Brittle-quasibrittle transition in dynamic fracture: An energetic signature. *Physical Review Letters* 104, 45501.
- Sharon, E., Fineberg, J., 1999. Confirming the continuum theory of dynamic brittle fracture for fast cracks. *Nature* 397, 333.
- Shi, X., Yao, W., Xia, K., Tang, T., Shi, Y., 2019. Experimental study of the dynamic fracture toughness of anisotropic black shale using notched semi-circular bend specimens. *Engineering Fracture Mechanics* 205, 136–151.
- Vasudevan, A., Grabois, T.M., Cordeiro, G.C., Morel, S., Ponson, L., 2021. Adaptation of the tapered double cantilever beam test for the measurement of fracture energy and its variations with crack speed. *arXiv preprint arXiv:2101.04380*.
- Viesca, R., Garagash, D.I., 2017. Numerical methods for coupled fracture problems. *Computational Methods in Applied Mechanics and Engineering*.
- Wada, H., Seika, M., Kennedy, T.C., Calder, C.A., Murase, K., 1996. Investigation of loading rate and plate thickness effects on dynamic fracture toughness of PMMA. *Engineering Fracture Mechanics* 54, 805–811.
- Wan, K.T., Lathabai, S., Lawn, B.R., 1990. Crack velocity functions and thresholds in brittle solids. *Journal of the European Ceramic Society* 6, 259–268.
- Wrobel, M., Mishuris, G., 2015. Hydraulic fracture revisited: Particle velocity based simulation. *International Journal of Engineering Science* 94, 23–58.
- Xing, Y., Huang, B., Ning, E., Zhao, L., Jin, F., 2020. Quasi-static loading rate effects on fracture process zone development of mixed-mode (I-II) fractures in rock-like materials. *Engineering Fracture Mechanics* 240, 107365.
- Xu, X., Jeronimidis, G., Atkins, A.G., Trusty, P.A., 2004. Rate-dependent fracture toughness of pure polycrystalline ice. *Journal of Materials Science* 39, 225–233.
- Zhang, Q.B., Zhao, J., 2013. Effect of loading rate on fracture toughness and failure micromechanisms in marble. *Engineering Fracture Mechanics* 102, 288–309.
- Zhao, Y., Gong, S., Hao, X., Peng, Y., Jiang, Y., 2017. Effects of loading rate and bedding on the dynamic fracture toughness of coal: laboratory experiments. *Engineering Fracture Mechanics* 178, 375–391.